# RESEARCH AND DEVELOPMENT OF SUPER LIGHT WATER REACTORS AND SUPER FAST REACTORS IN JAPAN

Y.Oka[1], S.Morooka[1], M.Yamakawa[1], Y.Ishiwatari[2], S. Ikejiri[2], Y.Katsumura[2], Y.Muroya[2],
T.Terai[2], K.Sasaki[2], H.Mori[3], Y.Hamamoto[3], K.Okumura[4],T.Kugo[4],T.Nakatsuka[4],
K.Ezato[4],N.Akasaka[4,] A.Hotta[5]

[1] Waseda University, Tokyo, Japan, [2] University of Tokyo, Tokyo, Japan
[3] Kyushu University, Fukuoka, Japan, [4] Japan Atomic Energy Agency, Ibaraki, Japan
[5] TEPCO Systems Corp., Tokyo, Japan

## Abstract

Super Light Water Reactors (Super LWR) and Super Fast Reactors (Super FR) are the supercritical-pressure light water cooled reactors (SCWR) that are developed by the research group of University of Tokyo since 1989 and now jointly under development with the researchers of Waseda University, University of Tokyo and other organizations in Japan. The principle of the reactor concept development, the results of the past Super LWR and Super FR R&D as well as the R&D program of the Super FR second phase project are described.

## 1.        Introduction

Supercritical water does not exhibit a change of phase. The water density decreases continuously with temperature. The heat is efficiently removed at the pseudo-critical temperature, which is approximately 385°C at 25MPa. The advantages are the compactness of the plant system due to the high specific enthalpy of supercritical fluid, the simplicity of the plant system without the recirculation system and dryers of BWRs and steam generators of PWRs and high thermal efficiency without the limit of the boiling temperature.

The objective of the Super LWR design study is to develop power reactor concepts in meeting the challenges of market economy by reducing capital cost based on the experience of LWR and supercritical coal fired power plant technologies. The objective of Super FR design study is to develop fast reactor concept of lower capital cost than the thermal reactors such as LWR and Super LWR.

Water cooled fast reactors require the tight fuel lattice. The once-through coolant cycle is compatible with the tight lattice core of water cooled fast reactors. The increase in the core pressure drop due to the tight lattice does not cause problems with pumping power and stability because of the low coolant flow rate of the once-through cycle and small difference of water densities between the "steam" and the "water" at the supercritical pressure.

The plant system of the Super FR is the same as that of the Super LWR, a thermal reactor. Fast reactors do not need a moderator. Their power density is inevitably higher than that of the thermal reactors. High power density is an advantage in economy. The Super FR has higher power density than the Super LWR. The Super LWR is expected to show better economy than LWRs due to the compactness, simplicity of the plant systems and high thermal efficiency. The Super FR will be better than LWR and Super LWR from the compactness.

Experimental R&D is carried out for developing the data base of thermal hydraulics, materials and coolant interactions with materials. It is mainly funded by the "Super fast reactor" projects that was/is entrusted by MEXT. The first phase was conducted between December 2005 and March 2010.The second phase started in August 2010. The results are common data base for the fast option (Super FR) and thermal option (Super LWR).

## 2.      Principle of the reactor concept development

The Super LWR and the Super FR are the new reactors that were not constructed before. The optimum reactor designs are not known. Simply applying LWR components and the systems to Super LWR and Super FR is not a good way in achieving the goal of capital cost reduction. Both PWR and BWR in the early days were not the same systems as the present ones. It took some years to reach optimized plant designs. LWR components and systems are optimized for LWR and not optimized for Super LWR and Super FR.

Important physical phenomena are identified by the computer simulation quantitatively in relation with the goals and criteria. Priorities of experimental R&D items of Super FR projects are determined from the results. It reduces the time and cost of R&D. If the goals and criteria are not satisfied, the design is changed slightly and modeled by computer programs. The improvement is evaluated quantitatively.

 "Pursuing simplicity" is the good principle guiding the optimization of SCWR design. For example, when the simplest design of core cooling, the "one path core" where whole core coolant flows upward did not satisfy the goal of the 500C reactor outlet coolant temperature, the design was slightly made complicated such as the two pass core where the peripheral core was cooled by downward flow and the central core was cooled upward flow in series. The improved design is quantified by the computer simulation.

Priorities of thermal- hydraulic R&D items were also determined based on the quantitative evaluation of the effects on the reactor performance. The computational fluid dynamics, CFD method is extensively used for the analysis such as the behaviors of coolant flows in fuel channels.

## 3.      Super LWR design

### 3.1.      Improved core design

Super LWR is the supercritical pressure light water cooled and moderated reactor with the reactor pressure vessel (RPV). It was developed by the research group of University of Tokyo since 1989. The design and analysis of Super LWR is summarized in the monograph, "Super Light Water Reactors and Super Fast Reactors" that was published in July 2010[1]. It includes overview of the studies, core design, plant system design, plant dynamics and control, plant startup and stability, fast reactor design and research and development. It includes the published results before 2009.

Peak cladding temperature is the important parameter for the integrity of the fuel cladding. It should be maintained during abnormal transients. The evaluation procedure is summarized in Fig.1. The maximum peak cladding temperature is the base temperature for the safety analysis. It is evaluated by taking the radial and axial flux factors, local flux factors and engineering uncertainties into account.

The radial and local flux factors were evaluated separately, but further improvement was made. Incorporating sub-channel analysis into the three-dimensional core calculation, iterating the sub-channel analysis with the core calculation rationalizes the evaluation of radial and local flux factors. The nominal peak steady state temperature decreases 25°C from the value of the separate evaluation of Fig. 1.

The spacing between fuel rods of the first core of the Super LWR was 1mm to keep the coolant velocity in the fuel channel high enough to remove heat in spite of the low coolant flow rate of the once-through cycle. In order to decrease the sensitivity of the maximum cladding temperature to the engineering uncertainties of the spacing, the core with 2mm fuel rod spacing was designed [2]. The improved core design with the 2-mm fuel rod spacing was studied with rationalization of the core design method. The sub-channel analysis was iterated with the three-dimensional core design. The local flux factor effect on cladding temperature was incorporated in the core design. The cladding temperature at the nominal peak steady state condition of the new core with 2-mm fuel rod spacing decreased 12°C, even if the average coolant flow rate in the fuel channel decreased 27%. The core height was increased slightly from 4.2m to 5m not to decrease the coolant flow rare in the fuel channel substantially. The characteristics of the core with 2mm spacing are compared with that of 1mm spacing in Table. 1.

### 3.2.     Revised start-up procedure

The turbines of the Super LWR and the Super FR and their startup will be similar to or the same as for of FPPs where the turbines are warmed and started using subcritical pressure superheated steam generated by super-heaters. However, the Super LWR and the Super FR have no super-heater and it is difficult to generate superheated steam in the core due to concern about fuel damage by the dryout. A startup loop with a pump and a steam drum is used instead of the additional heater. This revised startup system is shown in Fig. 2. The Super LWR and Super FR adopt the once-through coolant cycle like FPPs without a circulation loop. Since it is difficult to raise the pressure and temperature in the once-through cycle, however, a circulation loop, just for startup, is added to the Super LWR and the Super FR plant. Since the Super LWR and Super FR have no pressurizer heater, nuclear heating is chosen for raising the pressure and temperature in the loop. The circulation loop for startup consists of the reactor, the steam drum, the heat exchanger ("cooling system"), the circulation pump and the piping.

### 3.3     Transient sub-channel analysis

The cross flow between sub-channels is considered in the steady-state thermal hydraulic design using the steady-state sub-channel analysis code. On the other hand, the deterministic safety analyses are performed using the single channel code with an assumption that the relative mass flux distribution in a fuel assembly at abnormal conditions is the same as that at a steady-state condition. There is a concern that the distribution may change at abnormal conditions, especially flow decreasing conditions, due to the change in the pressure drop distribution. A transient sub-channel analysis code is developed and applied to representative flow decreasing events, an abnormal transient and an accident, in order to

estimate whether and how much the safety margins to the criteria of the cladding temperature change from the results obtained with the single channel code [4].

For the verification of this code, three typical steady-states are calculated and compared to the results by the steady-state sub-channel analysis code. Table 2 summarizes the three steady-state cases. The steady-state conditions are obtained using the transient code by making all the parameters converge after a sufficiently long enough calculation time. For each case, the distributions of the cladding surface temperature at the axial position having the highest temperature are compared between the steady-state and transient codes. They agree very well.

As representative flow decreasing events, the "partial loss of reactor coolant flow" and the "total loss of reactor coolant flow" are analyzed. The former gives the highest increase in the cladding temperature among the flow decreasing transients analyzed by the single channel code. The latter gives the highest increase in the cladding temperature among the flow decreasing accidents, excluding the small LOCA, analyzed by the single channel code.

The time profiles of the increase in the maximum cladding surface temperature (ΔMCST) at the partial loss of reactor coolant flow are shown in Fig. 3. The peak values of cases 1 and 2 are almost equal to that calculated by the single channel code while that of case 3 is higher than the result by the single channel code by about 25°C.

The time profiles of the ΔMCST at total loss of reactor coolant flow are shown in Fig. 4. The same tendency as in the "partial loss of reactor coolant flow" is obtained although both the ΔMCST and the temperature difference in the fuel assembly are higher for this accident. The highest ΔMCSTs for Cases 1 and 2 are almost equal to that calculated by the single channel analysis while that for Case 3 is higher than the single channel result by about 140°C. It should be mentioned that the Super LWR still has a margin to the limitation of the ΔMCST although it decreases from 290°C to 150°C by considering the cross flow.


## 4.      Development of Super FR concept

The purpose of this development is to clarify quantitatively the advantage of high power density of fast reactors over thermal reactors to achieve economic competitiveness of fast reactors. The concept of Super FR was developed mainly by numerical simulations. The studies covered fuel and core design, plant control, start-up, stability, plant heat balance, and safety analysis [5]. It was conducted with the funding of Super FR R&D project phase1 between 2005 and 2010 that was entrusted by the ministry, MEXT.

In the fuel rod and core design, MOX and stainless steel cladding are used for seed fuel rods. Depleted UO2 and stainless steel cladding are used for blanket fuel rods. The fuel rod parameters are determined to satisfy thermal, fluid-dynamic and mechanical criteria and also to achieve high power density and high average outlet temperature. In the blanket assembly, the fuel rod region is surrounded by a solid moderator (ZrH layer) so that fast neutrons coming from the seed fuel slow down in the ZrH layer and are absorbed by the blanket fuel without causing fast fissions. It enables the Super FR to have a negative void reactivity without adopting flat core shape or additional devices.

The core characteristics, the cross sections of the core and the fuel assemblies, the reactor pressure vessel and coolant flow and the plant system are described in the reference [5]. Comparison with the characteristics of BWR and PWR is shown in Table.3. Comparison of the primary containment vessels (PCV) of the Super FR and a PWR is shown in Fig.5

## 4.2    Safety analysis
The results of safety analysis of the Super FR are shown in Fig.6. All events satisfied the criteria. Total loss of coolant flow is the most limiting accident. The improvement of design for increasing the margin is planned in the second phase of Super FR project.

## 4.3    High temperature structural design
The reactor coolant temperatures are 500C at the outlet and 280C at the inlet. The reactor pressure vessel and the internal structure are exposed to high stresses during the transients. The structural design was improved based on the stress analysis. A seal pipe is connected between reactor outlet coolant nozzle and the upper plenum. It reduces the thermal stress during transients [Fig.7]. The inelastic stress analysis of the nozzle was conducted. Thermal stress ratchet, creep ratchet and elastic-plastic creep were evaluated. The structural design of the tie plates and the support plate of the upper plenum was also improved from stress analysis.

## 4.4    CFD Analysis of tight fuel bundle
It is difficult to measure circumferential temperature distribution of the tight fuel lattice of 1mm spacing experimentally. It was analyzed by the computational fluid dynamics (CFD) code. The radial temperature distribution was 11C, when the heat conduction of the fuel cladding was taken into account [Fig. 8]. It decreases when the fuel rod diameter decreases from 7mm to 5mm with keeping the 1mm spacing. The coolant temperature decreases at the corner and edge sub-channels facing the fuel assembly duct wall, when the same spacing (1mm) as between the fuel rods. The ratio of the heated perimeter to the sub-channel area needs to be kept uniform throughout the fuel assembly for making the coolant temperature distribution flat.

The effect of difference of fuel rod power on the cladding temperature distribution was not large. Fig.9(a) gives the computational model of seven fuel rods bundle considering displacement. The effect of the displacement of the center fuel rod (rod A) on the heat transfer is evaluated. As shown in Fig. 9(a), the displacement of fuel rod A in the angle range of $30°$ can stand for this case. Heat conduction in the cladding is considered. MCST with different displacements is summarized in and Fig.9(b), MCST increases exponentially with the displacement. MCSTs of cases with displacement angle of $30°$ are larger than those of $0°$ because the gap clearances between fuel rods A and C of cases with displacement angle of $30°$ are larger than those of $0°$ under the same displacement. But the difference is very small as the relative displacement is smaller than 1%. The relative displacement should be less than 1% if the allowable increment of MCST due to displacement is less than $6°$. The relative displacement should be less than 2% if the allowable increment of MCST is less than $10°$.

## 4.5    ACE-3D code development
For potentially replacing large-scale experiments for developing the fuel bundles in the future R&D, the existing 3-D CFD code "ACE-3D", which has been developed by JAEA based on the two-fluid model, was enhanced to handle the supercritical-pressure fluids in the fuel bundle geometry. The heat transfer experiments of Kyusyu University and JAEA were analyzed by this code for its validation.

Figure 10(a) shows the computational domain, which simulates the test section of the 7-rod test bundle heat transfer experiment performed by Kyushu University. In this analysis, one-twelfth of the area of the test section is adopted as shown in Fig. 10(a) to save the computational cost.

Figure 10(b) shows the wall temperature profiles of the simulated fuel rods at P1, P2, and P3 of Fig. 10(a). Calculation results are in agreement with experimental data. It was confirmed that ACE-3D can predict the wall temperature of the simulated fuel rod by including heat conduction in the simulated fuel rod.

## 4.6     Stability

Thermal and stability considerations during power-raising phase of plant start-up were analysed [7]. Since part of the seed fuel assemblies and all the blanket fuel assemblies of the Super FR are cooled by downward flow, the feedwater from the reactor vessel inlet nozzle to the mixing plenum located below the core is distributed among these fuel assemblies and the downcomer. The flow rate distribution as the function of both the reactor thermal power and the feedwater flow rate, which are the design parameters for the power-raising phase, is obtained by the thermal hydraulic calculations. Based on the flow rate distribution, thermal analyses and thermal hydraulic stability analyses are carried out in order to obtain the available region of the reactor thermal power and the feedwater flow rate for the power-raising phase. The criteria for the "available" region are the maximum cladding surface temperature (MCST) and the decay ratio of thermal hydraulic stability in three "hot" channels; two seed assemblies with upward/downward flow and a blanket assembly. The decay ratio of thermal- hydraulic stability during power raising phase is shown in Fig.11.

## 4.7     Transmutation analysis in relation with the backend risk study

The neutron spectra of the Super of FR core are compared with the liquid metal fast breeder reactor (FBR) and LWR in Fig12. The blanket fuel assembly of the Super FR includes 1cm thick zirconium hydride layer for making the coolant void reactivity negative at the loss of coolant events. The neutron spectrum of the blanket is very soft, similar to that of LWR. The transmutation capability of the Super FR was analyzed in relation with the backend risk, not simply neutronics points of view. The transmutation of not only minor actinides (MA), but long lived fission products (LLFP), was considered.

Both human risk and environmental risk need to be considered as the backend fuel cycle risks. The radiation dose rate and toxicity of the elements that were released into the environment were considered. Among the minor actinides from the 4N+1 series parent elements such as Np-237 and Am-241, Th-229 is the most important element from the toxicity. The minor actinides are also important for the heating rate of the high level radioactive waste.

Among LLFP, Cs-135 is the most important for the peak of radiation dose. The solubility into ground water is high. Ts-99 and I-129 are also important elements from the backend risk. The radiation dose rates of a solidizied high level waste canister are shown in Fig.13. The Cs-135 is the most influential at 20000 years and Th-229 is at $10^7$ years. The support factors of the Super FR for MA and TRU are 11.6 and 3.1 respectively. It means that the Super FR transmutes MA and TRU from 11.6 units and 3.1 units of PWR respectively. The support factors of the Super FR are 11.8 and 6.2 for Tc-99 and I-129 respectively, while they are 2.6 and 5.6 for LMFBR. The LLFPs are transmuted more effectively in the Super FR than LMFBR. Transmutation of Cs-135 is difficult due

to the small neutron capture cross section of Cs-135 and the generation from the neutron capture of Cs-133. Confinement and multi- recycling of Cs-135 in the fuel cycle will be one solution.

## 4.8     Methods developments
### 4.8.1     Evaluation of accuracy of the transmutation calculation
The transmutation calculation method was developed by Dr. Okumura of JAEA for the analysis. The calculation method for evaluating the error of transmutation rate calculation was also developed by him. The standard deviation of the errors of the transmutation rates due to the cross-section uncertainly of the major elements such as U-235, U-238, Pu-239, Pu-240, Pu-241 and Pu-242 were less than 1%.

The errors of MA elements depend mainly on the errors of the parent elements when MA is not loaded in the reactor. But the error depends mainly on the error of the capture cross section of the MA element itself when MA is loaded in the reactor. The error of Th-229 is 3.3% without the MA loading and 0.5% with the MA loading is the reactor. The nuclear data are based on JENDL-3.3.

The errors of LLFP generation were evaluated directly using sensitivity coefficients, since no covariance data are available. The error of Cs-135 generation is approximately 20%. The errors of Tc-99 and I-129 productions are 60% and 160%. The errors of transmutation rates of Tc-99 and I-129 were also evaluated and 15.1% and 32.5% respectively. The errors are governed by the errors of the capture cross sections.

### 4.8. 2     MPS method for the analysis of condensation of a steam bubble
Steam bubble condensation occurs when the steam is discharged into water. The dynamic load needs to be considered for the integrity of the containment. Bubble condensation is one of the key fundamental research issues in fields of two phase flow heat transfer as well as nuclear reactor thermal hydraulics. For numerical simulation, traditional mesh-based method such as finite difference method and finite volume method etc. are usually failed in accurately configuring the inconstant vapor-liquid interface because of severe distortion of interfacial computing cells.

Moving Particle Semi-implicit (MPS) method has advantages over traditional mesh-based methods in accurately configuring vapor-liquid interface. Single saturated and superheated steam bubble condensation behaviors in sub cooled water have been simulated by using MPS method. The liquid phase was described using discredited particles and the vapor phase was treated with using real gas state equation. The two phase interface was set to be movable saturated boundary which can be easily traced according to the movement of boundary particles. The interfacial heat conduction flux was determined according to the energy variation of interfacial liquid layer and the additional direct contact heat transfer between superheated steam and saturated interface has been taken into account for superheated case. The calculation was compared with the experiment. The change of the shapes and the bubble lifetime are compared [Fig.14]. Good agreement with the experiment was obtained [8].

## 5.     Thermal-hydraulic experiments
The fundamental thermal-hydraulic data base was developed by the experiments at Kyusyu University with the surrogate fluid (HCFC22). The heat transfer experiment of fuel rods was conducted at JAEA Naka laboratory with supercritical water loop for the verification of the data of Kyusyu University. The experiments were conducted as the 1st phase project of Super FR R&D, but

the results constitute common data base for the Super FR and Super LWR design and analysis. The picture of the experimental loop of Kyusyu University is shown in Fig.15. The pictures of the supercritical water loop of JAEA Naka laboratory and the 7- rods fuel bundle are shown in Fig. 16.

## 5.1     Thermal hydraulic experiments with the surrogate fluid
### 5.1.1    Single tube experiments
Both upward flow and downward flow were tested. The results were compared with the heat transfer correlations. Watts- Chou correlation showed the best agreement both upward and downward flows [Fig.17].

The change of the measured friction pressure drops with the mean bulk enthalpy of the fluid is shown in Fig.18 for upward and downward flow. It agrees well with the Itaya- correlation for unheated turbulent flow in a tube.

Onsets of departure from nucleate boiling (DNB) at subcritical pressure region close to the critical-pressure was measured during depressurization transient from the supercritical-pressure. The faster the depressurization, the longer the DNB continues. The maximum wall temperature is higher at high flow rate, but it is similar to the steady state value at low flow rate of the depressurization.

The heat transfer coefficients were measured at flow-reducing transients at the supercritical pressure. The deterioration of the heat transfer was mild at the flow decreasing transients.

### 5.1.2    7- rod bundle experiment
Heat transfer experiments of 7-rod bundle were conducted at steady state as well as transient conditions. The purposes are to compare the results with those of the single tube experiment, to prepare the heat transfer correlations for the bundle and pressure drop formula. The effect of the grid spacers was also evaluated. The first result was reported in 2008 [9].

The geometries of the 7-rod bundle and the test section are shown in Fig. 19. Four types of the bundles were tested by changing the shapes and distance of the grid spacers. The picture of the grid spacers are shown in Fig. 20. The effect of turbulence of the spacers was measured with the test apparatus of unheated nitrogen gas flows. The turbulence was measured at the center of the sub-channel in the downstream. The result is shown in Fig.21. The spacer with asymmetric blades showed large turbulence. It is effective in enhancing heat transfer. The measured local wall temperature and heat transfer coefficient of the bundle type I are shown in Fig. 22.

In every 10 kJ/kg bulk fluid enthalpy region, the heat transfer coefficient shows bumpy profiles. It decreases from high to low values. It is the effect of the grid spacers. The heat transfer coefficient is maximum just after the grid spacers and decreases. There is no difference was observed in the heat transfer coefficients in radial direction of the heater rods, such as in the middle of the sub-channel and at the minimum distances between the rods.

In the 7- rod bundle, the wall temperature is sensitive to the distance between the central rod and the circumferential rods. The average heat transfer coefficient is derived from the multiple measured wall temperatures at each axial position. The average wall temperature and heat transfer coefficient for upward and downward flow of bundle Ⅱ is compared in Fig. 23. The heat transfer coefficient is higher for the upward flow than the downward flow. It was observed for all four types rod bundles.

It is the effect of the grid spacers. The heat transfer correlations for the rod bundles were prepared based on the measurements. The correlation for upward flow of the bundle type Ⅲ is as follows

$$Nu_b = 0.0039 \, Re_b^{0.95} \overline{Pr}^{0.57} \left( \frac{\rho_w}{\rho_b} \right)^{0.42} \left( \frac{\overline{C_p}}{C_{pb}} \right)^{0.02}$$

Where

$$Nu_b = \frac{\alpha D}{\lambda_b}, \quad Re_b = \frac{GD}{\mu_b}, \quad \overline{c_p} = \frac{h_w - h_b}{T_w - T_b}, \quad \overline{Pr} = \frac{\mu_b \overline{c_p}}{\lambda_b} = \frac{\mu_b}{\lambda_b} \cdot \frac{h_w - h_b}{T_w - T_b}$$

The comparison with the measurements is shown in Fig. 24. It agrees with the 240 measured data within 10% variance.

The friction pressure drops of the rod bundles were measured. The pressure drop of the type 4 grid spacers was the highest. It induced the highest heat transfer among the four types of spacers. The formulas of total friction pressure drops of the bundle type 2.3.4 were prepared from the measured pressure drops and the Ishigai's friction formula for tubes. It is compared with the measured data in Fig. 25. It agrees with the experiment within 10%.

In order to understand of the characteristics of the critical heat flux condition near the critical pressure, the critical heat flux at the near-critical pressure was measured for vertically upward flow in the bundle channels, as well as in the circular tube [10]. Based on the experimental data, characteristics of the critical heat flux were clarified, including the maximum wall temperature and critical enthalpy changes with pressure, effects of the heat flux and mass velocity, the difference between pressure- increasing and pressure- decreasing processes, the comparison between the tube and bundle channels, and the comparison of measured data with predicting correlation. The critical heat flux condition tends to occur at near- critical pressure region.

At pressure decreasing events, the critical heat flux condition broadens out to lower pressure side. The maximum wall temperature for the bundle type 3 was lower than that of type 1 and 2. It is due to the shorter distance between the grid spacers of the bundle type 3. The maximum wall temperature for the bundle type 3 was lower than that of type 1 and 2. It is due to the shorter distance between the grid spacers of the bundle type 3.

The heat transfer coefficients were measured during flow decreasing transients for the rod bundles. The ratios of the heat transfer coefficients to the steady state values for the bundle type 2 are shown in Fig. 26. The ratio is less than unity for the mass velocity of 700 kg/ (m²s). It is due to the higher heat flux coefficient at the steady state from the suppression of the heat transfer deterioration in the rod bundle.

### 5.1.3   Critical heat flux experiment at subctritical- pressure

The maximum wall temperature and the critical enthalpy were measured at steady state critical condition by changing the pressure from sub-critical to supercritical. The pressure was changed stepwise both decreasing from the supercritical pressure and increasing from the subcritical pressure. The critical enthalpy is defined as the enthalpy at the axial position where the critical condition occurs. The maximum wall temperature profiles differ between the decreasing and the increasing pressure as shown in Fig. 27. The onset of the critical condition shows the hysteresis. At pressure

decreasing transients, the critical condition continues to the lower pressure region and the wall temperature is kept high. The hysteresis was also observed for the rod bundle experiments. The maximum heat transfer coefficients and the critical enthalpy at critical heat flux conditions are shown in Fig. 28. The experimental data of the tube and the rod bundle 1 and 2 are compared. The maximum wall temperature is smaller for the bundle 2 than the bundle 1. There is no critical heat flux correlation that is applicable in the pressure region near critical pressure. New critical heat flux correlations were prepared for the tube and the rod bundle type 1 and 2. The result is compared with the measured data for the rod bundle type 2 in Fig. 29. The agreement is good, within $\pm 0.3$.

### 5.1.4    Critical flow measurement
The discharge of supercritical fluid into air was measured using HCFC 123 as the surrogate fluid. The result is compared with calculations [Fig. 30]. The flow rate was calculated as reversible adiabatic one-dimensional critical flow that the flow rate is limited by the sound speed at the discharge point. The solid lines show at critical flow and the dotted lines show at vertical flow and the dotted lines show subsonic flow. The agreement with the calculations is good. It is better for the calculation using the physical data of the HCFC123 itself. The sharp peak of the experimented data between 500 and 600s and slow rise before it were observed. The reason is not yet clarified.

### 5.1.5    Condensation experiment
Condensation behavior and the pressure generation need to be understood at the discharge of the supercritical water into the pool for the mechanical design of the containment and the pressure suppression pool. The pressure amplitudes were measured by changing the subcooling of the pool fluid. The experiment was done using HCFC123 as the working fluid. The pressure amplitude shows a peak as shown in Fig 31. It is the same behavior as the condensation of the steam at subcritical- pressure. The pictures of the condensation were taken by a high- speed camera. From the pictures of the cross section area of the condensing bubble, the frequency of the pressure vibration was calculated. It agrees well with the frequency of the pressure vibration at the condensation. It is concluded that the pressure vibration is due to the periodic change of the condensing bubble volume. The pressure amplitudes of the condensation between the subcritical and supercritical fluid are compared in Fig.32. No difference of the amplitude is observed.

## 5.2    Heat transfer experiments with supercritical water
Heat transfer tests with supercritical-pressure water were carried out at JAEA to verify the results obtained from the tests with HCFC22. A single heater rod and a 7-rod bundle with grid spacers, which are the same type as those of the loop of the Kyushu University for HCFC22, were tested [11].

The evaluations of heat transfer coefficients are concentrated on the comparison between heat transfer coefficients at the surface facing the sub-channel center and those at the surface in the narrowest gap region between rods. From the results, the difference of heat transfer coefficients at the both surfaces was not observed [5].

## 6.    Materials and water chemistry
This subject consists of developments of the fuel cladding material, the thermal insulation material and the methodology for measuring the dissolution of in-core materials into the coolant.

## 6.1    Fuel cladding material

Based on the advanced austenitic stainless steel (15Cr- 20Ni) developed by JAEA for the sodium cooled fast reactors, the candidate materials for the fuel cladding of the Super Fast Reactor have been manufactured and tested. The Ti-added advanced 15Cr-20Ni steel and the Zr-added advanced 15Cr-20Ni steel are produced experimentally. The materials are called advanced 15Cr-20Ni, Ti-added 15Cr-20Ni and Zr-added 15Cr-20Ni respectively in this paper.

From these materials, solution heat treated plates and 20% cold-worked fuel cladding tubes were prepared. The outer diameter, the thickness and the length of the tube were 5.5mm, 0.4mm and 2000mm respectively. Three types of the cladding tubes were prepared by changing the cold- work condition as Q values of 2.4, 1.2 and 0.5. The condition of solution heat treatment of the plates was 1120℃ and 15 minutes for Ti-added ones and 1100℃ and 15 minutes for Zr- added ones. That of the cladding tubes was 1120℃ and 5minutes. The compositions of the materials are shown in Table 4.

High priority is given to high temperature strength (including creep strength) and corrosion resistance. Tensile tests up to 750°C and creep tests up to 700°C were conducted at JAEA. Corrosion tests in supercritical water up to 600°C were conducted at JAEA and University of Tokyo Resistances to stress corrosion cracking (SCC) and swelling are also important. Slow strain rate tests (SSRT) have been conducted at JAEA.

The strength of the plates and the tubes were evaluated by tensile and creep testing. The tensile test was conducted at room temperature, 600, 650, 700 and 750C. The temperature of the creep testing was 600 and 700C. The testing periods were 2000 hours for the plates and 1000 hours for the cladding tubes. From the testing data, the creep strength during the service life was estimated using the Larson-Miller parameters. The results for the cladding tubes are depicted in Fig. 33.

Corrosion testing in water was conducted. Ti and Zr-added 15Cr-20Ni as well as the irradiated advanced 15Cr-20Ni for sodium cooled fast reactor were exposed at the high pressure condition (600C, 25MPa, 8ppm). The water is circulated. The testing period was 2000 hours for the plates and 1000 hours for the cladding tubes.

Slow strain rate tests (SSRT) was conducted for BWR conditions for these materials at the high pressure and high temperature conditions for assessing the sensitivity of stress corrosion cracking. For comparison, commercial SUS316L, SUS310S, and non-irradiated standard 15Cr-20Ni steel that was taken from the wrapper tube of the sodium cooled fast reactor were also tested as well as the Ti and Zr added 15Cr-Ni steels.

The oxidation layer was formed on the surface of all tested materials. There was no apparent difference in the formation of the layers between the materials. No ablation of the layer was observed. The weight gain and loss before and after the removal of the layer were measured. The results are shown in Fig.34 for BWR conditions and Fig. 35 for supercritical conditions. The Zr-added 15Cr-20Ni showed good corrosion resistance behaviors. The thickness of saturated corrosion layer was estimated less than 1 $\mu$ m. The SEM images of the surface and cross-cut area were taken. It was observed that the oxidation layer of the Zr-added 15Cr-20Ni was smaller than others.

The corrosion behavior of the cladding tube was also tested up to 1000 hours at BWR condition and the supercritical water condition. The result of supercritical water condition is shown in Fig.36. Both

weight gain and weight loss of the cladding tubes are smaller than the plate materials. This is due to effect of the dislocation at the cold work of the tubes. The diffusion of chromium to the surface was enhanced by the dislocation. The SEM images ware also taken after the corrosion testing. The oxidation layer is thinner than those of the plate materials.

Among the materials that were tested by slow strain rate test (SSRT) at BWR conditions, only the neutron irradiated advanced 15Cr-20Ni showed the inter-granular stress corrosion cracking (IGSCC). The fraction of IGSCC area was 27% of the cross section of the fracture. The un-irradiated advanced 15Cr-20Ni as well as the Zr-added one did not show the sensitivity to IGSCC. The cause of IGSCC is not from cold-working, but may be the effect of neutron irradiation or thermal aging.

In conclusion, Zr-added 15Cr-20Ni advanced austenitic steel looks promising fuel cladding material. The further testings are required for the optimization of the cladding tube production, long- term corrosion behaviors and neutron irradiation and its effect on the corrosion behaviors.

## 6.2    Thermal shielding material

Thermal insulations are necessary for the coolant guide tubes in the upper plenum and water rod walls due to large temperature difference between the coolant inside and outside. The requirements for the thermal insulator are low heat conductivity, small neutron absorption, and good mechanical strength and dimensional stabilities. The candidate materials were surveyed from the existing database and porous Yttria-Stabilized Zirconia (YSZ) was selected from the neutron absorption and swelling properties [12].

The fabrication of YSZ was studied. The pore former sintering temperature and micro-structure were controlled. Its effects on the density, pore diameter and the conductivity were clarified. Poly-meta-acrylate (PMMA) was used as the pore former. The thermal conductivities of 3mol% $Y_2O_3$ added zirconia (8YSZ) are shown in Fig.37. The sintering density was 25%. The thermal conductivity is very low, about 1/20 of the zirconia. But its compressive strength needs to be verified for the reactor use.

The linear expansion coefficients of 3YSZ and 8YSZ were measured [Fig.38]. The liner thermal expansion coefficient does neither depend on the density nor sintering temperature. The stability against thermal cycling was also verified by testing.

The compressive strength of YSZ was studied. It depends on the density, grain size, sintering temperature, pore diameter etc. The compressive stress of 8YSZ was maximum for PMMA diameter was 0.8 $\mu$ m, when the sintering temperature was 1300C. The compressive strength of 8YSZ is shown in Fig.39. The compressive strength of 8YSZ with 25% density (75% porosity) is too low to be used in the reactor. The 8YSZ of 40% density (60% porosity) is necessary for use in the reactor of 25MPa pressure with margin.

The stability of 8YSZ and 3YSZ was tested by immersing them into the pure water at supercritical pressure (300-500C) at 25MPa for 300-500 hours. The 3YSZ was turned out not stable in the water. It became fragmented into powder. The 8YSZ was stable in the water. The phase transition to tetragonal to monoclinic occurred in the 3YSZ during the testing. The structure of the 8YSZ remains mostly tetragonal.

The change of the thermal conductively of 8YSZ with the density is depicted in Fig.40. The data of 8YSZ of 50% density will be the reference for use in the Super FR and Super LWR.

It is concluded that 8YSZ of the density above 40% is suitable for the thermal shielding material for Super LWR and Super FR.

## 6.3    Elution characteristics of stainless steel

It is very important to understand the elution characteristic of structural stainless steels in supercritical-pressure water in order to manage turbine contamination. A new approach was developed to evaluate the elution characteristic of stainless steels in supercritical-pressure water [13]. Radio-activated specimen (SUS304) with a known radioactivity is used as sample and set at an autoclave vessel in a supercritical water loop system. By measuring gamma-ray emitted from the eluted material, the elution can be quantified with high sensitivity. The test condition is from 300 to 550C, 25MPa and dissolved $O_2$ concentration ranges from 0 to 400 ppb (Fig. 41).

In de-aerated water, the results show that the elution rate at any temperatures decelerated with increasing time in spite of progress of corrosion on the surface of stainless material. Furthermore, it was found that, compare to the result obtained at 300℃, the elution efficiency at 550℃ becomes much lower, even the corrosion rate increasing. As for 200ppb $O_2$ experiment, the elution rate and the relative elution efficiency show a similar decrease with increasing temperature, except for the elution rate at 300℃ being a constant at least up to 500 hours. On the other hand, at 550℃, the elution at 200ppb $O_2$ was obviously higher than that at de-aerated water. The elution efficiency was higher at dissolved hydrogen (DH) and de-aerated conditions at 300C. The formation of protective oxygen layer may suppress the elution.

Time behavior of elution by increasing the temperature from 300C to 550C at 100hour is shown in Fig.42. The elusion was suppressed at 550C. The solid line shows the result of keeping the temperature unchanged, 300C. It shows that the elution continues. The formation of protective oxide layer may suppress the elution as shown in Fig.41. But the sudden suppress of the elution at increasing the temperature to 550C is not simply explained by the formation of the oxide layer.

The time behaviors of decreasing the temperature from 550C to 300C are shown in Fig.43. The elusion increases after decreasing the temperature. The elusions at 550C were almost kept constant. But the elution was small when the period of keeping 550C is long.

Time behavior of elution at different pretreatment condition before decreasing the temperature to 300C is show in Fig.44. The elusion is small for the pretreatment at the high temperature of 550C. The change of elution for different oxide layer thickness is shown in Fig.45. This is the result in the de-aerated water for 500 hours. The thickness of the layer was estimated by Auger electron measurement.

In conclusion, elution behavior changes with the temperature. At the high temperature such as 550C, the solubility of oxides and physical property of water suppress the elution. At the low temperature as 300C, the formation of protective oxide layer suppress the elution. The thickness of the layer affects the elution at the low temperature. In reducing environment such as dissolved hydrogen (DH) and de-aerated conditions the formation of sub-micron protective layer suppress the elution, not

depending on the temperature. In oxidizing environment such as 200ppb and 400ppb dissolved oxygen (DO) conditions, the formation of the layer does not necessarily suppress the elution.

Combining the understanding of the elution experiments with that of corrosion testing, the followings are derived,
1. Elution of radioactive elements such as cobalt has correlation with that of iron and not with the elution of nickel and chromium. Suppressing elution of iron will suppress that of cobalt.
2. In reducing environment of water, the formation of surface layer suppresses the elution of cobalt without depending on the temperature. The main composition of the oxide layer will be $NiFe_2O_3$ (nickel-spinel) at 300C and $Fe_3O_4$ (magnetite) at 550C.
3. In oxidizing environment the formation of oxide layer does not necessarily suppress the elution of iron and elution of cobalt continues at 300C

But under supercritical water condition, the solubility and physical property of water govern the elution. The elution is small. But at high oxidizing condition such as 400ppb at 550C, the ablation of the layer and re-absorption make the protective layer non-uniform. The elution from the thin protective layer may continue.

## 7.    Super fast reactor R&D project (2nd phase)
The second phase started in August 2010 and will continue until March 2013. The followings are the subjects.
(1) Development of the plant concept:
- Core design
- Safety analyses
- Experiment on the reactivity effects of a zirconium hydride layer
(2) Thermal-hydraulics:
- Freon experiments
- Water experiments
- CFD simulations
(3) Material-coolant interactions:
- Experiment on corrosion product transport
- Experiment on high temperature oxidation in steam.
The member organizations involved in the project are Waseda University, University of Tokyo, Kyushu University, Tohoku University, JAEA, Advanced Industrial Science and Technology and TEPCO systems.

## 8.    Conclusion
Conceptual design and analysis of Super LWR and Super FR were conducted at the University of Tokyo. The results are summarized in the book "Super Light Water Reactors and Super Fast Reactors". Pursuing optimum design are the most challenging and important, because no one knows it. Computer simulation was extensively used for quantifying the ideas and designs. It was also useful to find out import physical behaviors quantitatively for the design and R&D. It is a new way of reactor development.

Thermal hydraulic (TH) experiments and materials R&D are conducted under the project of "Super fast reactor". Fundamental TH database and the materials were developed. The results will be useful for the development of not only Super FR but also Super LWR.

## Acknowledgements

## 9.      References

[1]      Y. Oka, S. Koshizuka, Y. Ishiwatari and A. Yamaji, "Super Light Water Reactors and Super Fast Reactors", Springer, (2010)

[2]      M. Kadowaki, "Rationalization of core design method and improved core design of Super LWR", Master thesis, University of Tokyo (2009) (in Japanese)

[3]      S. Yamada et al., "Design and analysis of procedures for system pressurization and line-switching to once-through mode in plant start up of SCWR", Proc. NURETH-13, Kanagawa, Japan, September 27- October 2, 2009, NBP1435(2009).

[4]      K. Yoshimura, et al., "Development of transient subchannel analysis code of Super LWR and application to flow decreasing events", ibid, NBP1434 (2009).

[5]      T. Nakatsuka et al., "Current status of research and development of supercritical water cooled fast reactor (Super fast reactor) in Japan", IAEA Technical Meeting on Heat Transfer, thermal- hydraulics and systems design for supercritical pressure water cooled reactors, 5 to 8 July 2010, Pisa, Italy(2010).

[6]      J. Gou et al., "CFD analysis in tight-lattice sub-channels and seven-rods bundle geometries of a super fast reactor", Proceedings of ICAPP'09, Tokyo, Japan, May 10-14, 2009, paper 9262 (2009).

[7]      Jiejn Cai et al., "Thermal and stability considerations for a supercritical water-cooled fast reactor with downward-flow channels during power-raising phase of plant startup". Nucl. Eng. Design, vol.239, pp.665-679 (2009).

[8]      Weixi Tian et al., "Numerical computation on thermally controlled steam bubble condensation using MPS method", Proceeding of the 4<sup>th</sup> International Symposium on Supercritical Water Cooled Reactors, March 8-11, 2009, Heidelberg, Germany, paper No.05 (2009).

[9]      H. Mori et al., "Research and development of a super fast reactor, (7) heat transfer to a supercritical pressure fluid flowing in a sub-bundle channel", Proc. 16<sup>th</sup> PBNC, Aomori, Japan, Oct. 11-18, 2008, paper ID-P16P1297 (2008).

[10]      H. Mori et al., "Experimental study for research and development of a super fast reactor, (1) critical heat flux in the near-critical pressure region", Proceeding of ICAPP'09, Tokyo, Japan, May 10-14, 2009, paper 9368 (2009)

[11]      K. Ezato et al., "Heat transfer in a seven-rod test bundle with supercritical pressure water (1): Experiments" Proc. ICAPP'09, Tokyo, Japan, May 10-14, 2009, paper 9464 (2009).

[12]      K. Sasaki et al., "Micro structural control of cintered porous Yittria-stabilized zirconia as a durable thermal shielding material", Intn'l. J. Appl. Ceram. Technol., 6[3] 362-372 (2009).

[13] Z. Han and Y. Muroya. "Development of a new method to study elution properties of stainless materials in subcritical and supercritical water", Pro. 4<sup>th</sup> International Symposium on Supercritical Water-Cooled Reactors, March 8-11, 2009, Heidelberg, Germany, paper No.75 (2009).
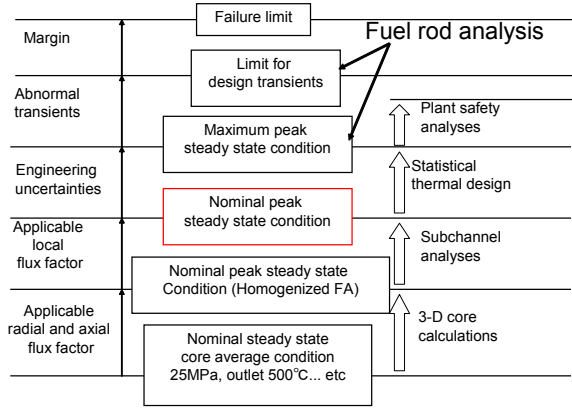
Fig.1 Evaluation of peak cladding temperature

Table 1 Improved characteristics of Super LWR core with 2mm fuel rod spacing

|  | Previous study | Present study |
|---|---|---|
| Core height/ Equivalent diameter [m] | 4.1/3.73 | 5.0/3.04 |
| Fuel rod gap clearance [mm] | 1 | 2 |
| Core pressure [MPa] | 25 | 25 |
| Core thermal output/Electrical output [MW] | 2744/1200 | 2352/1030 |
| Inlet/Outlet coolant temperature [℃] | 280/500 | 280/500 |
| Core coolant flow rate [kg/s] | 1418 | 1216 |
| Coolant average velocity in center blanket assembly [kg/m²/s] | 1206 | 883 |
| U235 enrichment Lower/Upper/Average [wt%] | 6.2/5.9/6.11 | 7 |
| Maximum cladding surface temperature(nominal) [℃] | 708 | 696 |
| MLHGR/Average linear heat rate [kW/m] | 38.9/18.0 | 38.8/18.0 |
| Average power density [kW/l] | 59.9 | 65 |
| Insulation material thickness (Material) [mm] | 2.0 (ZrO₂) | 1.0 (YSZ) |



Fig.2 Revised startup system of Super LWR and the Super FR

Table 2 Steady state conditions for transient subchannel analysis

|  | Case 1 | Case 2 | Case 3 |
|---|---|---|---|
| Radial power distribution | Flat | Typical one with control rods inserted | Typical one after control rods withdrawn |
| Axial power distribution | Cosine | Cosine | Top peak |
| Average linear heat rate [kW/m] | 18 | 18×0.7 | 18 |
| Inlet mass flux [kg/s/m²] | 739 | 739 | 739×1.3 |
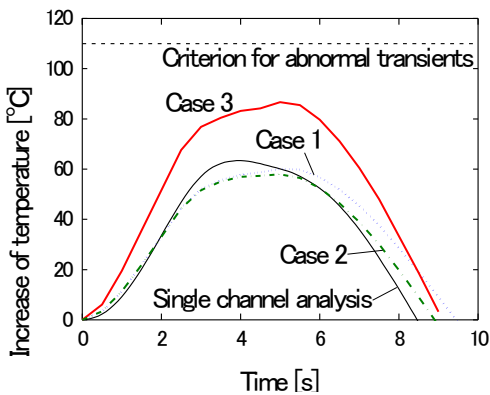


Fig.3 Profiles of the increase of maximum cladding surface temperature at partial loss of reactor coolant flow
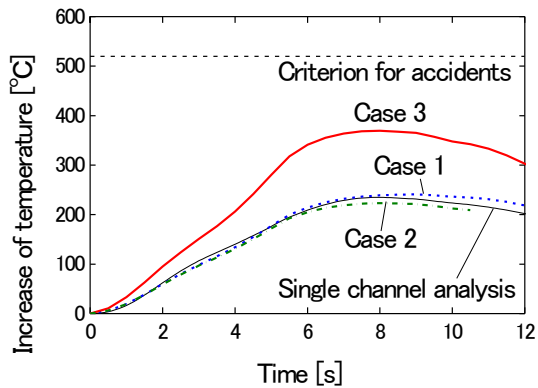


Fig.4 Profiles of the increase of maximum cladding surface temperature at total loss of reactor coolant flow

Table 3 Comparison of the characteristics between Super FR, BWR and PWR

|  | Super FR | ABWR | PWR |
|---|---|---|---|
| Reactor coolant system | Once-through cycle | Direct cycle with recirculation flow | Indirect cycle |
| Electrical output [MWe] | 700 | 1,356 | 890 |
| Thermal efficiency [%] | 44 | 34.5 | 33.4 |
| Core pressure [MPa] | 25 | 7.2 | 15.4 |
| Average power density [W/cm³] | 295 | 50.6 | 約100 |
| Inlet/Outlet coolant temperature [℃] | 280/508 | 216/287 | 284/321 |
| Flow rate [t/s] | 0.821 | 14.5 | 12.7 |
| Flow rate per electrical output [kg/s/MWe] | 1.17 | 10.7 | 14.3 |

|  | Super FR (700 MWe) | 2 Loop PWR |
|---|---|---|
| Cross section | | |
| I. D. Height Volume Footprint*1 | 27m 49m 22,500m³ 4,300m² | 40m 77m 67,900m³ 11,300m² |
| Components in PCV | ·RPV and relevant comp. ·Startup system ·SRV condensation tank | ·RPV and relevant comp. ·SG ·Pressurizer, condensation tank |

＊1 Footprint: Nuclear reactor area + turbine area

Fig. 5 Comparison of the primary containment vessel of Super FR and a PWR
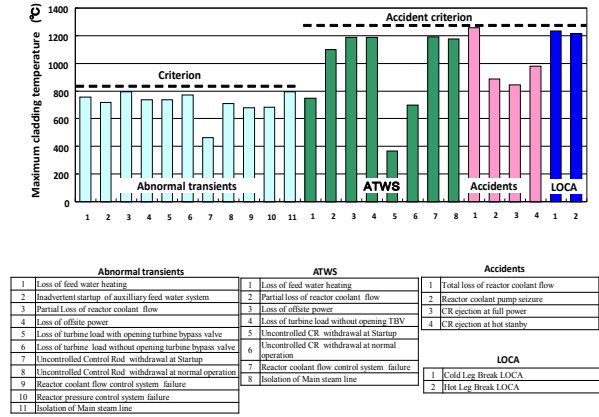
Fig. 6 Results of safety analysis of Super FR
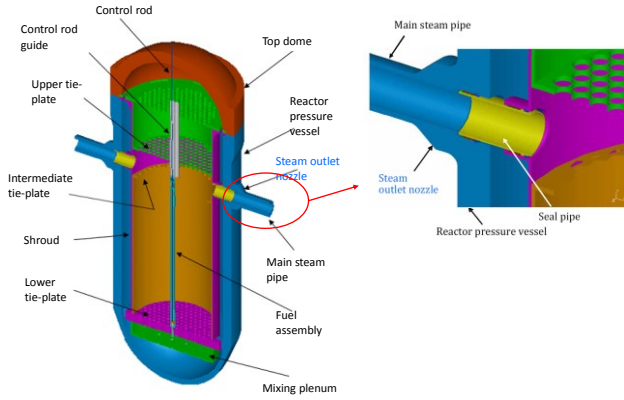


Fig. 7 Reactor pressure vessel



(a) Calculation model
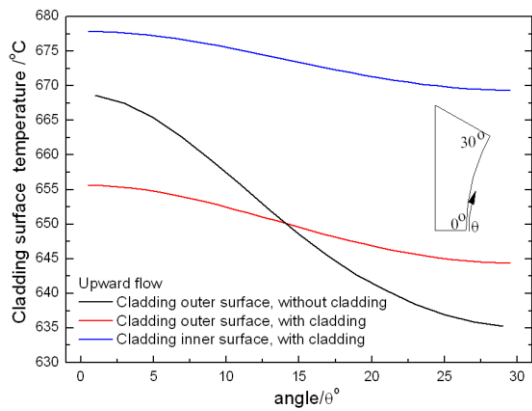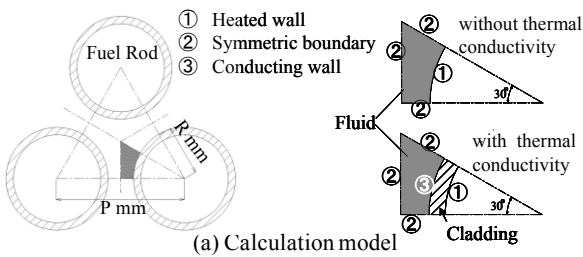


Fig. 8 Effect of heat conduction of cladding on circumferential temperature distribution
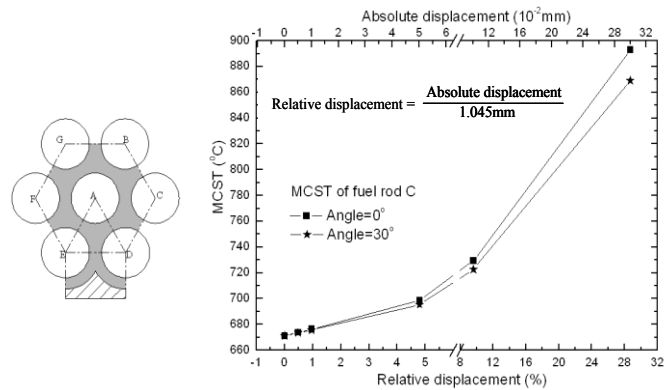


(a) Seven-rod bundle        (b) MCST with different displacement

Fig. 9 Calculation model of seven rod bundle and effect of the displacement of the central rod on the maximum cladding surface temperature (MCST)
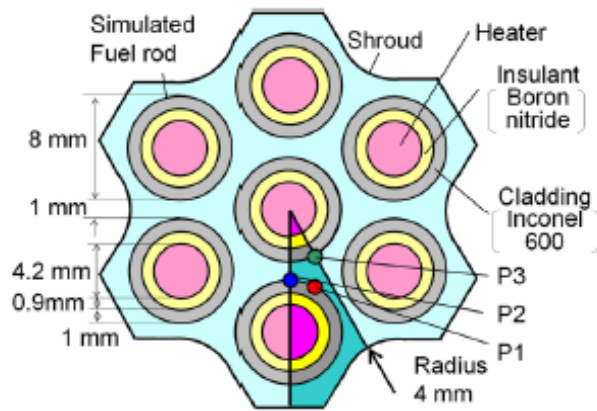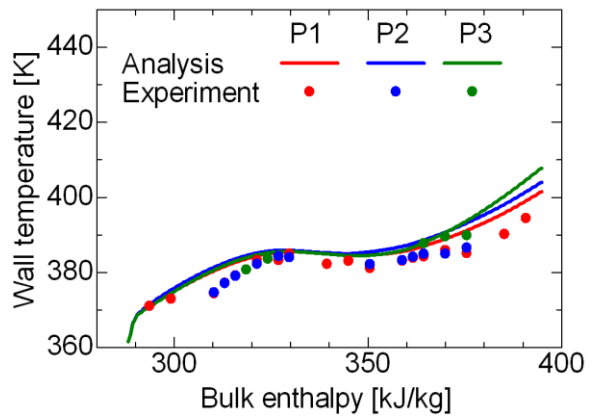


(a). Computational domain        (b)Comparison of Wall temperature profile between experiments

Fig. 10 Computational domain and comparison of wall temperature profiles between experiments and ACE- 3D calculation
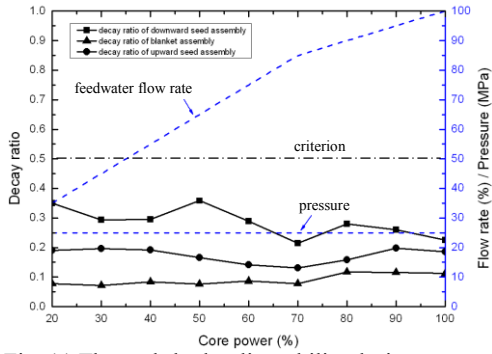
Fig. 11 Thermal- hydraulic stability during power rising phase
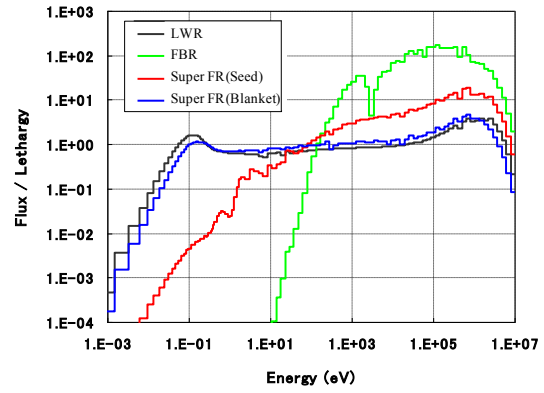


Fig. 12 The comparison of neutron spectra of Super FR (SFR) with those LMFBR (FBR) and LWR
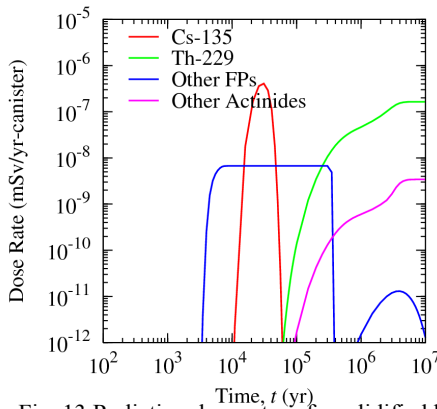


Fig. 13 Radiation dose rates of a solidified high level waste canister
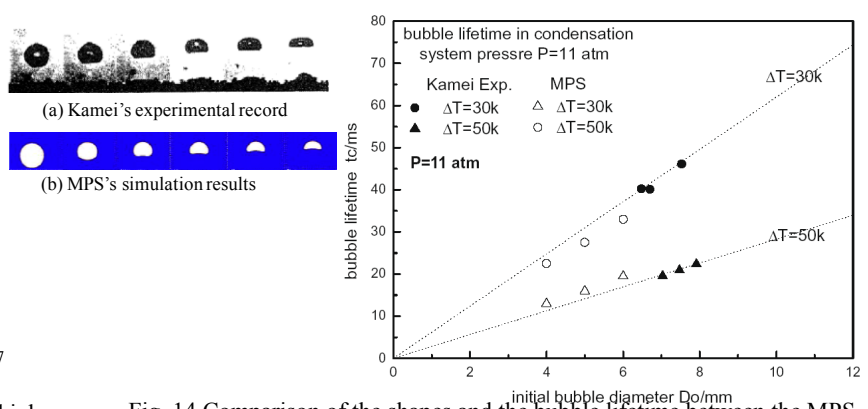


Fig. 14 Comparison of the shapes and the bubble lifetime between the MPS calculation and the experiment
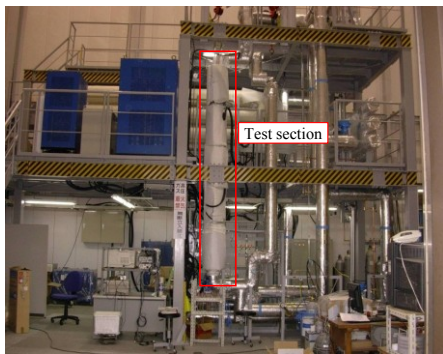


Fig. 15 The supercritical thermal hydraulic loop of Kyusyu University
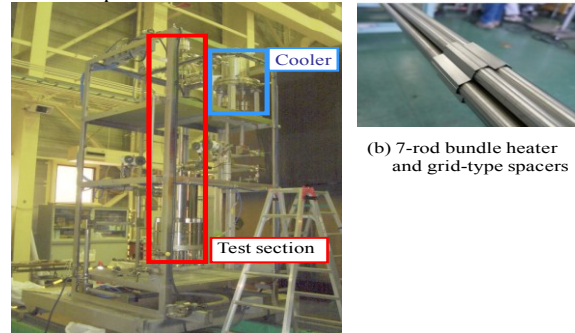


Fig. 16 The supercritical water loop of JAEA Naka-laboratory and 7-rod fuel bundle and the grid spacer
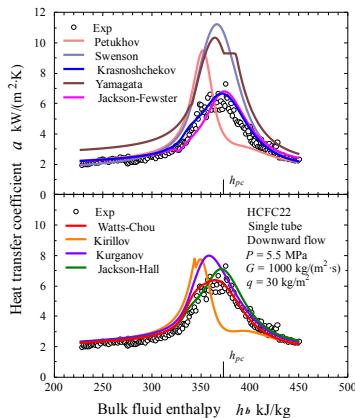


Fig. 17 Comparison of heat transfer coefficients of the downward flow with the correlations
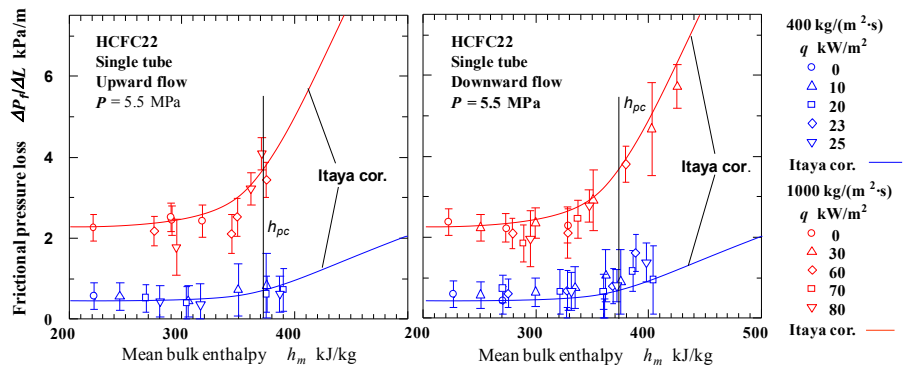


Fig. 18 Measured friction pressure drops of the single tube experiment and comparison with Itaya correlation

Fig. 19 7-rod bundle and the test section



(a) Bundle test section Ⅰ

Standard type

(b) Bundle test section Ⅱ, Ⅲ

Spacer with symmetrical blades

(c) Bundle test section Ⅳ

Spacer with unsymmetrical blades
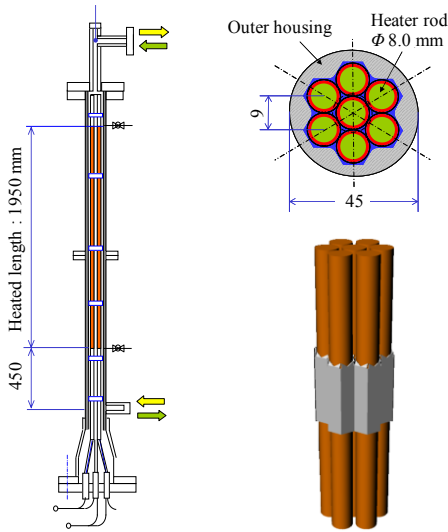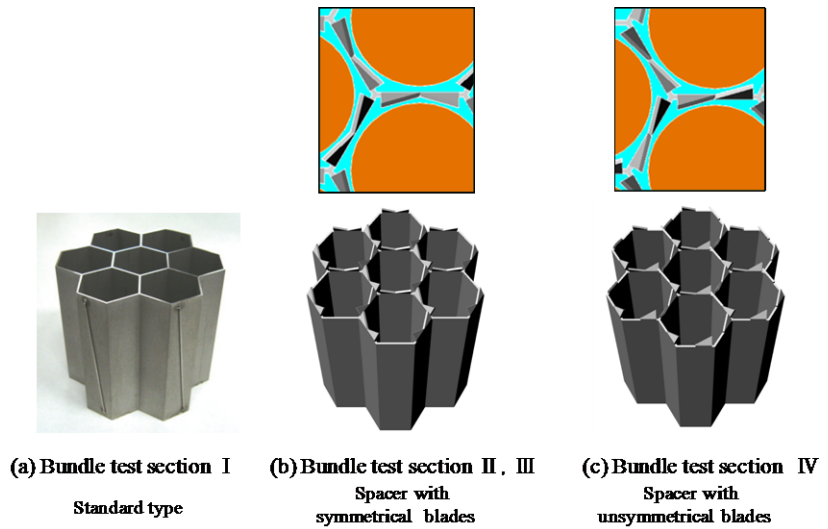
Fig. 20 Shapes of the grid spacers
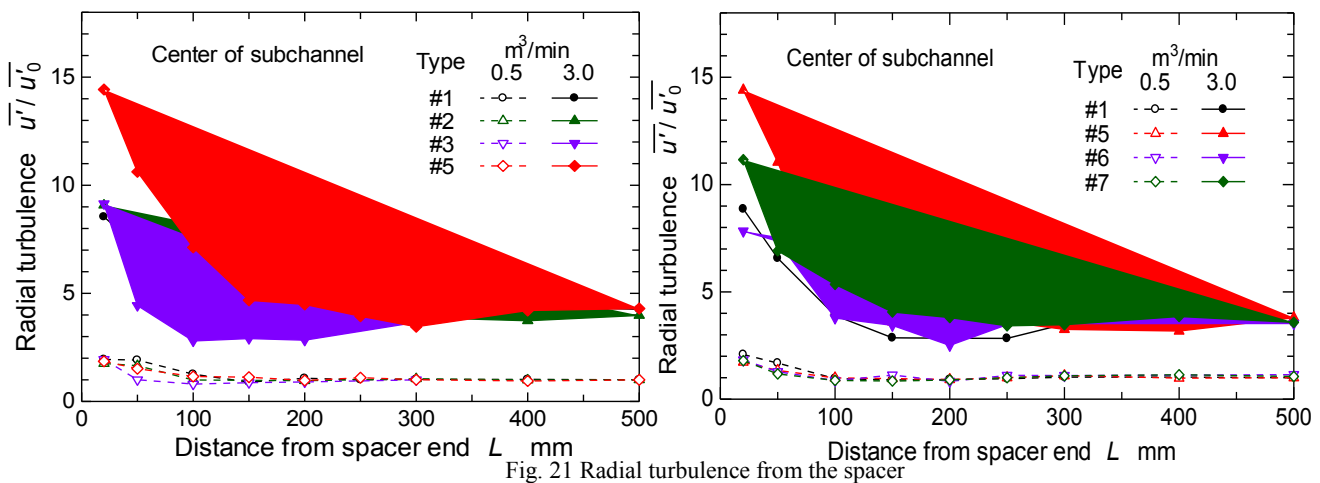


Fig. 21 Radial turbulence from the spacer
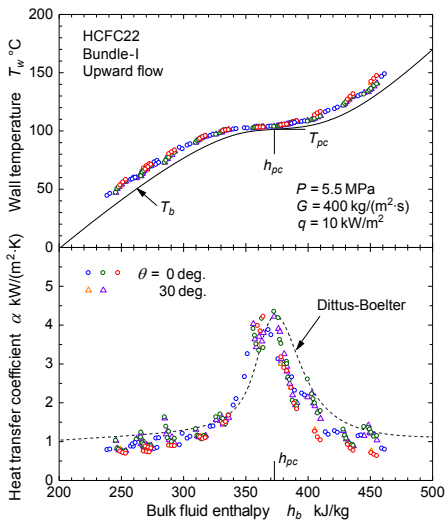


Fig. 22 Wall temperature and the heat transfer coefficient (bundle type Ⅰ)
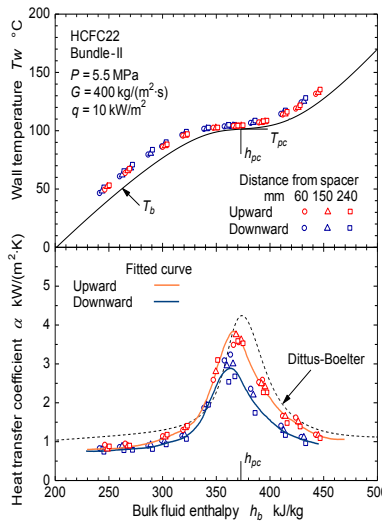
Fig. 23 Average wall temperature and heat transfer coefficient for upward and downward flow of bundle Ⅱ
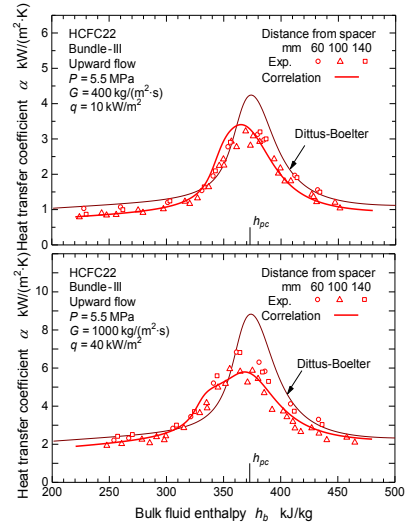
Fig. 24 Comparison of the measurement with the heat transfer correlation of the bundle type Ⅲ for upward flow
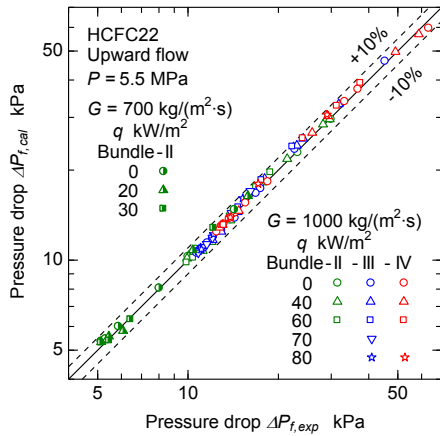
Fig. 25 Comparison of the measured pressure drops with the calculation by the formula for the rod bundles
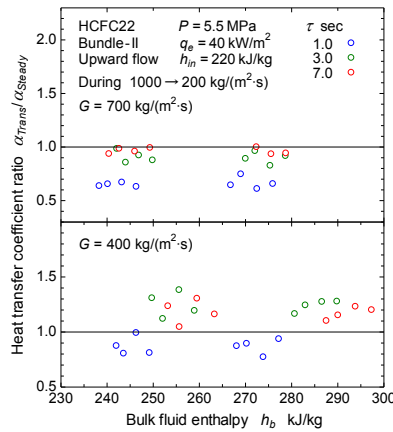


Fig. 26 Ratio of heat transfer coefficient during flow decreasing transients to the steady state values of the fuel bundle 2
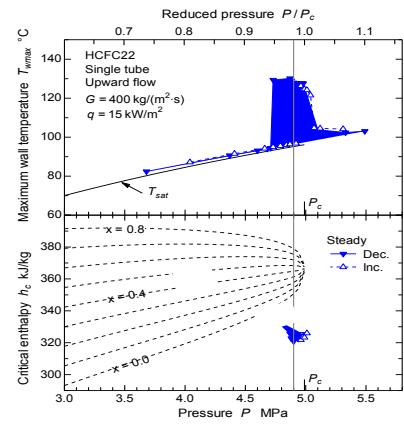


Fig. 27 Maximum wall temperature and the critical enthalpy for single tube experiment
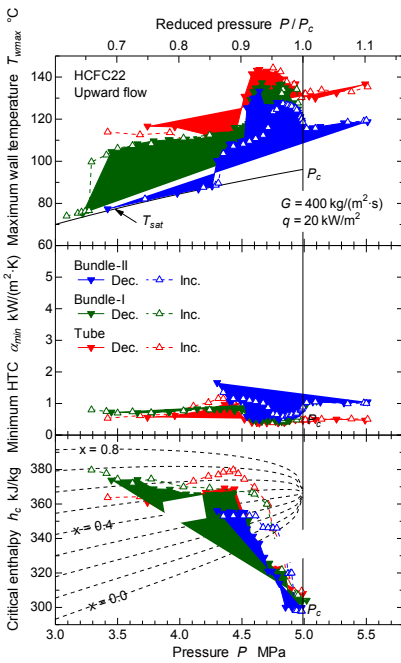


Fig. 28 Change of maximum wall temperature, minimum heat transfer coefficients and critical enthalpy with the pressure for single tube and the rod- bundles
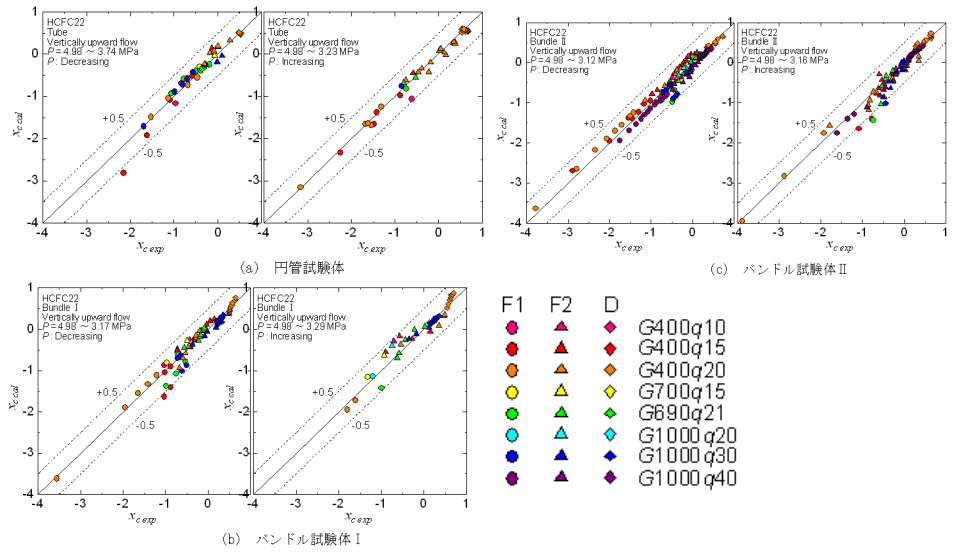


Fig. 29 Comparison of the measured critical quality with the calculation from the prepared critical heat flux correlations for rod bundle type 2.
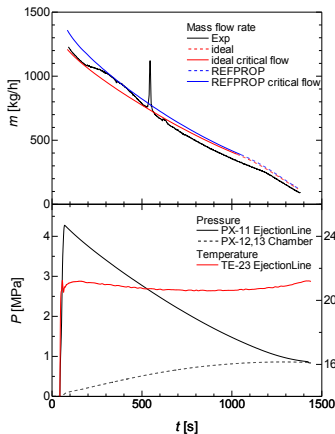


Fig. 30 The change of mass flow rate and pressure at the depressurization from the supercritical pressure and the comparison with the calculations
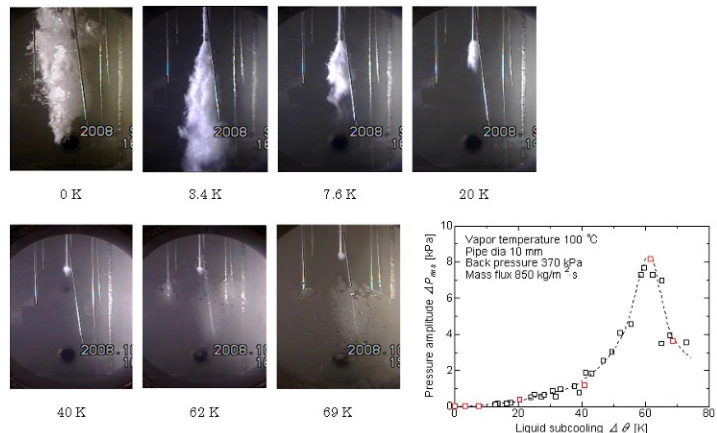


Fig. 31 The change of pressure amplitude with the liquid subcooling

(a)                                                (b)
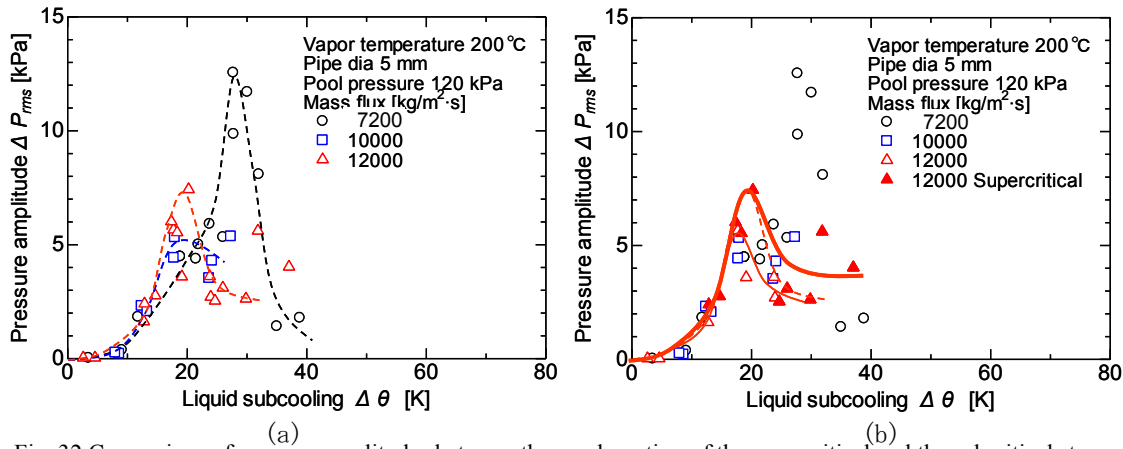
Fig. 32 Comparison of pressure amplitudes between the condensation of the supercritical and the subcritical steam

Table 4 Compositions of advanced austenitic stainless steel for fuel cladding

| Material | C | Si | Mn | P | Ni | Cr | Mo | Ti | Nb | B | Zr | Fe |
|---|---|---|---|---|---|---|---|---|---|---|---|---|
| Zr added 15Cr-20Ni | 0.061 | 0.79 | 1.68 | 0.026 | 19.98 | 15.26 | 2.45 | 0.24 | 0.10 | 0.0032 | **0.17** | Bal. |
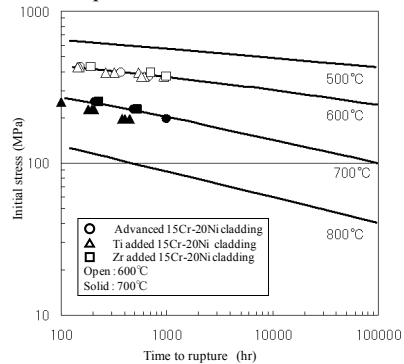


Fig. 33 Creep rapture strength of the advanced austenitic stainless steel cladding tubes
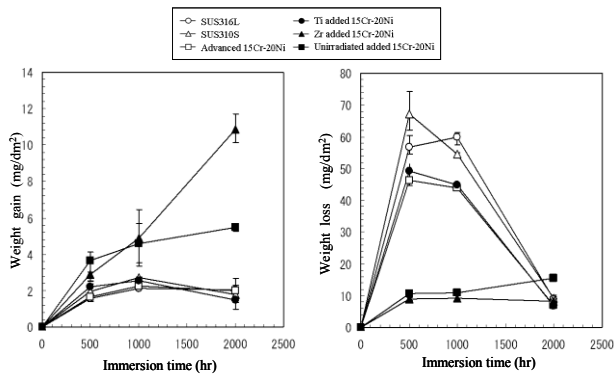


Fig. 34 Weight gain and loss of the plate materials before and after the removal of oxidation layer at a BWR conditions (210℃, 8MPa)
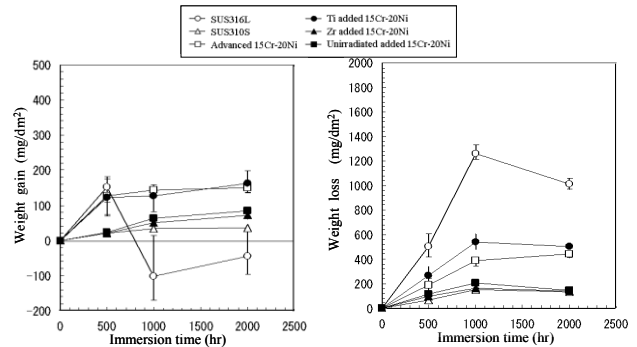


Fig. 35 Weight gain and loss of the plate materials before and after the removal of oxidation layer at supercritical water condition (600℃, 25MPa)
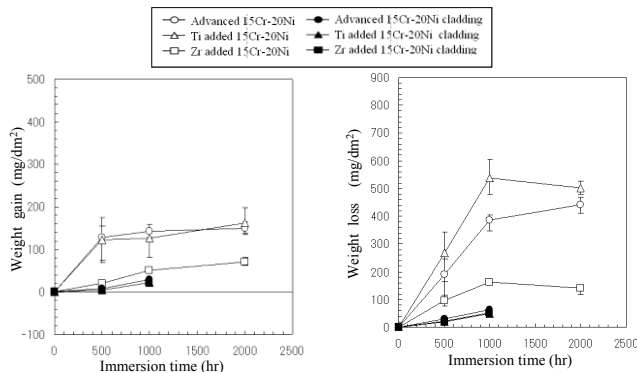


Fig. 36 Weight gain and loss of the cladding tubes before and after removal of oxidation layer at super critical water condition (600℃, 25MPa)
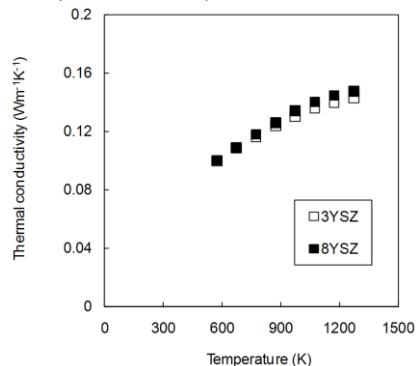


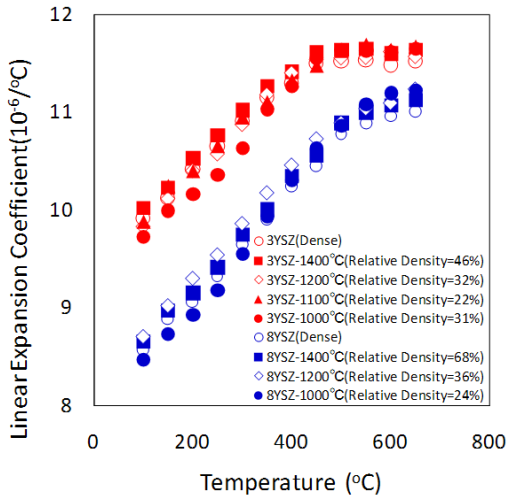Fig. 37 Thermal conductivity of the sintered porous 3 mol% YSZ (3YSZ) and 8mol%YSZ (8YSZ)
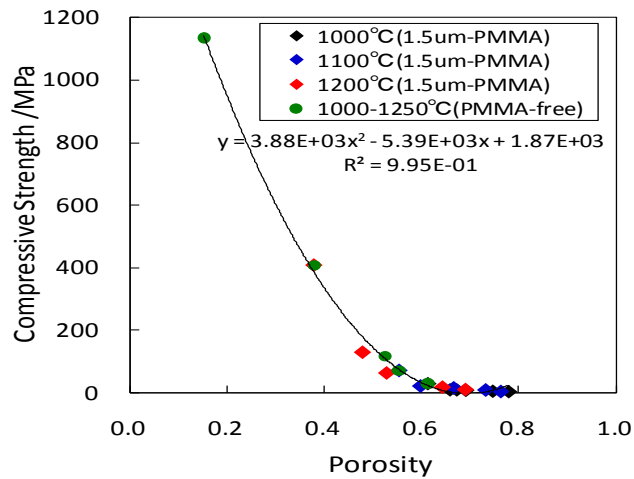
Fig. 38 Linear expansion coefficient of 3YSZ and 8YSZ

$$y = 3.88E+03x^2 - 5.39E+03x + 1.87E+03$$
$$R^2 = 9.95E-01$$
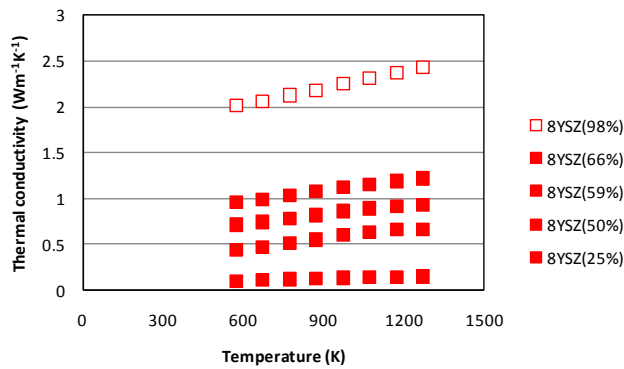
Fig. 39 Compressive strength of 8YSZ

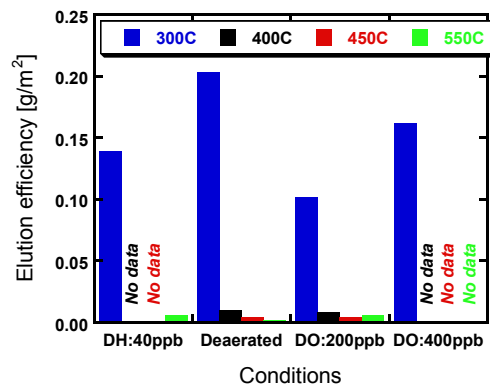Fig. 40 Change of thermal conductivity of 8YSZ with the density

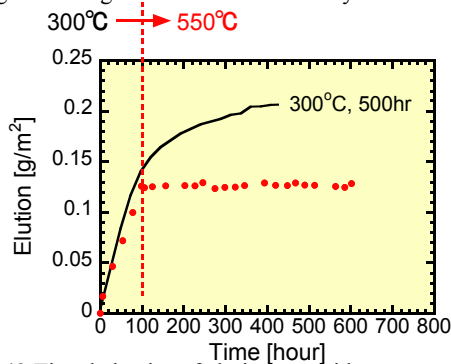Fig. 41 Effect of temperature and dissolved $O_2$ (DO) concentrations on the elusion amount at 500hr

Fig. 42 Time behavior of elution at rapid temperature increase in de-aerated water (solid line shows the result of constant temperature for reference)
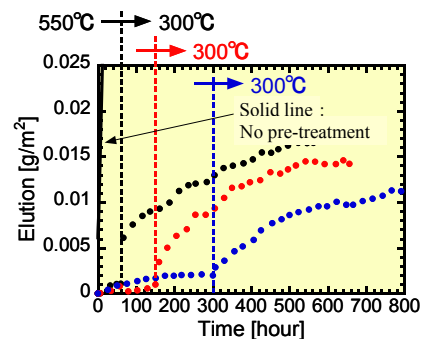
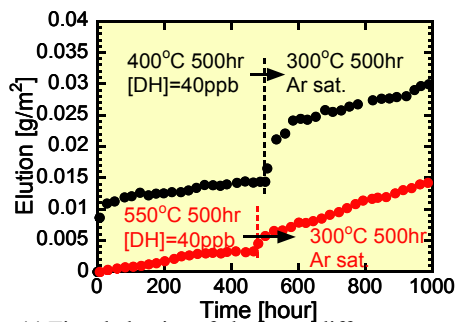Fig. 43 Time behavior of elution at rapid temperature decrease in de-aerated water

Fig. 44 Time behavior of elution at different pretreatment condition before decreasing the temperature to 300℃
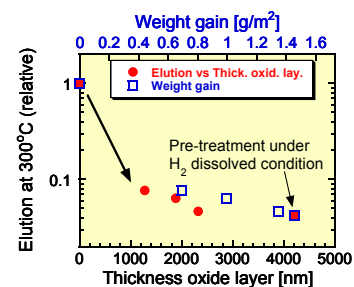
Fig. 45 Change of elution for different oxide layer thickness